Pattern formation in reverse filtration combustion

Chuan Lu* and Yannis C. Yortsos†
Department of Chemical Engineering, University of Southern California, Los Angeles, California 90089-1211, USA
(Received 20 January 2005; published 1 September 2005)

Using a pore-network simulator we study pattern formation in reverse filtration combustion in porous media. The two-dimensional pore network includes all relevant pore-level mechanisms, including heat transfer through the pore space and the solid matrix, fluid and mass transfer through the pore space, and reaction kinetics of a solid fuel embedded in the pores. Both adiabatic and nonadiabatic cases are considered, the latter modeled with the inclusion of heat losses from the pore network to the ambient. The simulation results show the development of unstable, fingered patterns of the burned fuel, similar to previously reported in the literature in the related problem of reverse combustion in a Hele-Shaw cell. We study the sensitivity of the patterns obtained on a number of parameters, including the Peclet number. The results on finger spacing and finger width are analyzed in terms of a selection principle, similar to that used in the theory for unstable Laplacian growth.

DOI: 10.1103/PhysRevE.72.036201 PACS number(s): 89.75.Kd, 47.20.Ma, 47.70.Fw, 44.30.+v

I. INTRODUCTION

Filtration combustion (FC) is a process of importance to a variety of applications, from the recovery of oil from oil reservoirs [1] to the processing of materials [2,3]. The process involves the combustion of a stationary fuel in a porous medium through the injection of an oxidizing agent. It can also serve as an example of a strong exothermic chemical reaction taking place in a confined geometry [4]. When ignition occurs at the gas inlet, reaction and thermal fronts propagate in the direction of the injected gas, and the process is referred to as forward FC. When it is on the opposite side, the fronts propagate in the direction opposite to the gas flow, and the process is reverse FC. Forward filtration combustion was addressed in detail in a companion paper [5]. The present work focuses on issues that arise in reverse filtration combustion.

An important feature of reverse FC is the existence of unstable fronts resulting into pattern formation [6–11]. Zik *et al.* [10] and Zik and Moses [11] presented experimental results of reverse combustion fingering instability in a Hele-Shaw cell, which occurs when a thin solid fuel contained between two parallel plates burns against a forced oxidizing convective flux. While not the same, the process studied by Zik and co-workers shares many common features with reverse FC, specifically the confined space, the dominance of mass and heat transfer and the absence of a flame. Provided that the parameters were in a suitable parameter space, two-dimensional (2D) fingering instability patterns of the solid fuel were found. Similar patterns were also observed in microgravity experiments [12]. While their origin reflects Laplacian growth [13,14], a full understanding of their dynamics is still missing, however. Linear stability studies have been performed for reverse FC, one for the case when there is no gas-phase product [7] and another for the case of infinitely large Lewis number [15]. The combined effects of heat and mass transfer, notably of heat losses to the surroundings, can lead to different patterns, depending on the parameter values. In some limiting cases, simpler stochastic models have also been developed that capture aspects of the unstable behavior. For example, Conti and Markoni [9] conducted Monte Carlo simulations of a simplified model for reverse FC without convection.

The objective of this paper is to address fully developed pattern formation in reverse FC using a pore-network model. For this purpose, we will use the model developed for forward FC in a companion paper [5]. To our knowledge, a numerical study of the patterns of reverse FC has yet to be done. The pore-network model circumvents the need to formulate a continuum model and the resulting introduction of ad hoc effective parameters. In recent years, simulation of processes at the pore-network level has become a very useful alternative for the understanding of a number of processes in porous media involving fluid displacement, reaction and transport [16]. In such models, the porous medium is represented by an equivalent network of sites and bonds, the geometrical and transport characteristics of which are related to the pore microstructure. Sites represent volume, bonds represent transport. In certain cases, pore-network models also represent the finite-difference analogues of a continuum description, with the important difference, that in the pore network formulation the process parameters have a realistic justification. In the past, pore-network models have mostly focused on problems under isothermal conditions. For example, isothermal reactive transport and flow has been addressed in a number of pore-network studies for a variety of applications [17–21]. More recently, extensions have tackled nonisothermal transport by considering a dual network, one for pores and throats and another for the solid matrix of the porous medium [22–24].

Filtration combustion is a complex process, as it involves the combination of fluid flow, mass transfer, chemical reaction, and heat transfer phenomena in the pore space and of heat transfer in the solid matrix. Because of its inherent complexity, corresponding studies of FC processes are rather

*Now at Los Alamos National Laboratory.
†Corresponding author. Electronic address: yortsos@usc.edu

sparse. Hwang *et al.* [2,3] pointed out that it is necessary to take into account key geometrical and topological features of the microstructure in the simulation of FC processes in heterogeneous media, and developed a corresponding pore-network model, emphasizing heat transfer (but in a gasless system). An analogous model, with emphasis on the percolation characteristics of FC, due to a disordered fuel distribution, was presented in Lu and Yortsos [25]. A complete model that accounts for all the relevant aspects of the process, including chemical reaction, fluid flow and mass and heat transport, was recently developed by the same authors to study forward FC [5]. The model is based on a dual pore-network model [22] and includes heat transfer in both the pore space and the solid phase. In addition, it includes heat losses to the ambient environment. As will be shown below, heat losses play an important role on pattern formation. Here, we will apply it to study the behavior of reverse FC in a 2D medium. The patterns obtained are analyzed using the approach of Zik and Moses [11], but also the more elaborate approach based on the selection principles for Laplacian growth, e.g., as discussed in detail in Pelce [13].

Because of their relevance to this work, we briefly summarize the key findings of Zik and Moses [11]. The authors postulate that the pattern formation in their experiments is controlled by the diffusional instability of the oxidant to the burning fronts. They characterized the fully developed patterns using two characteristic length scales, the width, w, of a finger and the distance, d, between two adjacent fingers. In their experiments they found that the distance d is a linear function of the inverse square root of the mass Peclet number, while the width of the finger is practically insensitive to the mass Peclet number in the instability regime, but depends on the rate of heat release and the heat losses. The mass Peclet number, defined as $\mathrm{Pe}=Vh/D$, where D is the mass diffusion coefficient, h is the thickness of the Hele-Shaw cell, and V the oxidant injection velocity, denotes the relative strength of convection over diffusion. Zik and Moses [11] used the following physical arguments to explain the experimental results: An overall mass balance on the injected oxidant (here oxygen) leads to the following relation between the front velocity U and the oxidant injection velocity

$$U\frac{w}{w+d}=AV, \tag{1}$$

where A is an effective stoichiometric coefficient. For low injection rates, the fingers grow under conditions of diffusion control. Under steady state conditions, they then postulated the qualitative relationship

$$U=\frac{D}{w+d}. \tag{2}$$

In dimensionless notation (superscript tilde) with characteristic length the Hele-Shaw cell thickness and characteristic velocity the oxidant velocity, these two equations can be rearranged to yield

$$\tilde{d}=\sqrt{\frac{\tilde{w}}{A}}\mathrm{Pe}^{-1/2}-\tilde{w}, \tag{3}$$

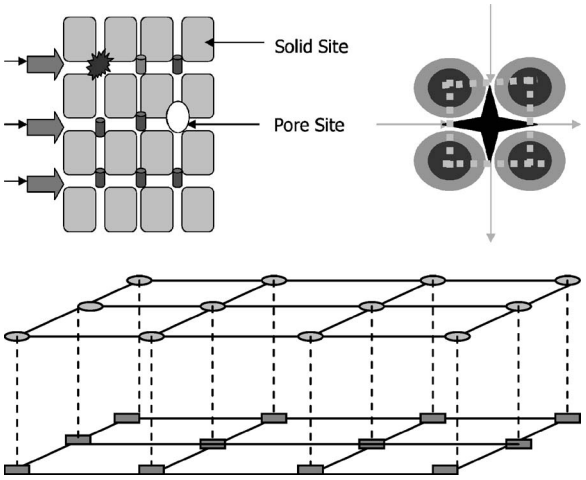

FIG. 1. The thermally coupled pore network and the inert solid matrix. (top) Schematic of the pore network; (bottom) the coupling between the pore network and the solid lattice. White denotes the pore network, black the inert solid. The dashed lines indicate pore-solid interactions. The one-to-one assignment between solid sites and pore sites is made for simplicity in the calculations.

$$\tilde{u}=\sqrt{\frac{A}{\tilde{w}}}\mathrm{Pe}^{-1/2}. \tag{4}$$

Further assuming that $\tilde{w}\approx 1$, Zik and co-workers [10,11] found that Eqs. (3) and (4) are in good agreement with the experimental results.

We will analyze the results to be obtained by using both the above approach and an extension of the solvability principles for Laplacian growth to the present problem. The paper is organized as follows. First, we describe the basic features of the pore-network model in Ref. 5 and the numerical method used for the solution of the governing equations. The model is then used to simulate reverse FC. We present the numerical results for a number of parameters, under both adiabatic and nonadiabatic conditions. We study numerically the sensitivity to a number of parameters, including the Peclet number, the strength of the heat losses and the effect of thermal conductivity. For a region of the parameter space, where diffusion of the oxidant is controlling, and conditions are nonadiabatic, the combustion front evolves in the form of patterns similar to the experiments of Zik and Moses [11]. To interpret the patterns, we will use a 1D theory for patterns that are quasi-one-dimensional. For fully developed fingering, we will test relations (3) and (4) but also present an alternative based on the solvability of Laplacian growth problems.

II. THE PORE-NETWORK MODEL

Consider a porous medium representation consisting of a network of sites (pores) and bonds (pore throats), embedded in a network of solid sites, representing the solid matrix [Fig. 1 (top)]. The solid fuel exists and chemical reactions occur in the pores, which are interconnected via throats. The latter control the transport of mass, momentum and heat. The solid network accounts for heat conduction in the solid matrix. In

the 2D simulations to be reported below, both networks are square lattices. Thermal coupling of the solid and the pore space occurs through heat transfer between pores and solid sites, as shown in Fig. 1 (bottom). Thermal coupling with the environment occurs through the sites. Important features of the model include the following:

(1) In 2D, each solid site communicates with four solid sites [Fig. 1 (bottom)] and one pore site [the dashed line between solid and pore sites in Fig. 1 (bottom)]. The solid sites interact with each other [depicted in Fig. 1 (bottom) by solid lines] via heat conduction, and with pore sites [the dashed line between solid and pore sites in Fig. 1 (bottom)] via heat transfer, through an effective heat transfer coefficient.

(2) The one-to-one assignment between solid sites and pore sites [for example, contrast with Fig. 1 (top)] is made for simplicity in the calculations. This representation is typical of two interacting phases. Relaxing it is straightforward but not necessary.

(3) Injection of oxidant (for example, oxygen) and inert gas occurs at one end, where pressure, temperature and composition are specified. The outlet end is at constant pressure. Dankwerts-type boundary conditions (zero gradients in temperature and concentration) are applied at that end. For the present case of reverse FC, ignition occurs at the end opposite to injection.

(4) Fluid flow in the pores is governed by Poiseuille's law.

(5) A one-step heterogeneous reaction is assumed,

$$\text{Solid fuel} + \mu(\text{gas oxidant}) \rightarrow \text{solid product} + \mu_2(\text{gas product}), \quad (5)$$

where μ and μ_2 are mass-weighted stoichiometric coefficients. In this paper, focus is only on the case for which there is zero net production of moles in the gas phase. The reaction is assumed heterogeneous, the rate expressed by the one-step kinetic model

$$R = k_r A_r C_g X_o H(V_f) \exp\left(-\frac{E_a}{RT}\right), \quad (6)$$

where k_r is the pre-exponential kinetic constant, A_r is the gas-fuel interface area in an individual pore site, C_g is the gas-phase concentration, X_o is the mass fraction of the oxidant, H is the step function, V_f is the volume of fuel, and E_a is the activation energy. In the above formulation, reaction kinetics have been vastly simplified to a one-step reaction to allow for a manageable numerical solution. This assumption is not uncommon for problems of this type of complexity.

(6) Within a pore site, thermodynamic equilibrium is assumed, and concentrations, pressure and temperature are uniform. This assumption is consistent with the pores and throats representation taken. Relaxing the assumption would require the much more complex problem of discretization of the entire pore space, which is outside our scope. Heat transfer does take place between adjacent pore sites, between pore and solid sites and between adjacent solid sites. Thermodynamic and transport parameters are taken constant. This assumption can be relaxed readily.

The governing equations express mass, momentum, and energy balances at the sites of the two lattices. They are as follows.

Balances on pore site i, adjacent to pore sites denoted by j: Gas-phase component k mass balance,

$$\frac{\Delta\left(\frac{P_i V_i}{RT_i} y_{i,k} M_k\right)}{\Delta t} = -\sum_j u_{ij} r_{ij}^2 \frac{P_i y_{i,k}}{RT_i} M_k - \frac{D_e}{lR} \sum_j r_{ij}^2 \left(\frac{P_i + P_j}{2}\right) \times \left(\frac{2}{T_i + T_j}\right)(y_{i,k} - y_{j,k}) + \mu_k \left[k_r A_i^r \frac{P_i y_{i,O_2}}{RT_i} \exp\left(-\frac{E_a}{RT_i}\right)\right] H(V_{i,f}). \quad (7)$$

Fuel balance,

$$\rho_f \frac{\Delta V_{i,f}}{\Delta t} = k_r A_i^r \frac{P_i y_{i,O_2}}{RT_i} \exp\left(-\frac{E_a}{RT_i}\right) H(V_{i,f}). \quad (8)$$

Energy balance,

$$\frac{\Delta E_i}{\Delta t} = -\sum_j u_{ij} r_{ij}^2 \frac{E_{g,i}}{V_i} - \frac{\lambda_{gs}}{l} \sum_j r_{ij}^2 (T_i - T_j) - h_s \sum_s A_{is}^h (T_i - T_s) - h_{L,P} A_{i,l}^h (T_i - T_0), \quad (9)$$

where we defined the energy content of a site as

$$E_i = E_{f,i} + E_{g,i},$$

$$E_{f,i} = \rho_f v_{f,i} (C_{p,f} T_i + \Delta_c H_f), \quad E_{g,i} = \sum_k \frac{P_i V_i}{RT_i} M_k y_{i,k} (C_{pg,k} T_i + \Delta_c H_f). \quad (10)$$

Momentum balance,

$$u_{ij} = \frac{r_{ij}^4}{8\kappa l} (P_i - P_j). \quad (11)$$

Energy balance on solid site s, adjacent to solid sites denoted by s and pore sites denoted by j: Solid site energy balance,

$$\rho V C_{ps} \frac{\Delta T}{\Delta t} = -\frac{\lambda_s}{l} \sum_{s'} A_{ss'}^h (T_s - T_{s'}) + h_s \sum_j A_{js}^h (T_j - T_s) - h_{L,s} A_{s,l}^h (T_s - T_0). \quad (12)$$

Before we proceed further, we note the following:

(i) In the above, we allowed for a volumetric heat loss to the surroundings, expressed through the heat transfer coefficient $h_{L,s}$. This is consistent with the assumed 2D representation of the problem. The effect of the heat losses to pattern formation is significant and will be particularly examined.

(ii) Ideal gas behavior is assumed, consistent with the high temperatures expected.

(iii) Poiseuille-type laws are assumed for the momentum balance. At the continuum level, this is equivalent to Darcy's law, an assumption often made in the literature. More importantly, because of the assumed linearity in the flow-rate

TABLE I. Nomenclature and typical values used in the standard case.

Variable	Notation	Typical values
Temperature	T	Ambient 373 K
Pressure	P	Outlet 1.01×10^5 Pa
Bond length	l	5×10^{-4} m
Bond radius	r	$l/2$
Porosity	φ	1/3
Site reaction surface	A_i^r	l^2
Site heat transfer surface with surroundings	$A_{i,l}^{\ h}$	l^2
Site heat transfer surface with solid	$A_{i,s}^{\ h}$	l^2
Pore site volume	V	φl^3
Solid volume	V_s	$3(1-\varphi)l^3/4$
Pure fuel volume	V_f	$(1-\varphi)l^3/4$
Pure fuel density	ρ_f	840 kg/m^3
Solid density	ρ_s	840 kg/m^3
Reaction rate	$k_0=k_r\exp(-E_a/RT^*)$	2×10^6 kg m/mol s
Activation energy	E_a	120000 kJ/kmol
Heat of reaction	$\Delta_r H$	11200 kJ/kg
Stoichiometric coefficient	μ	1.0
Stoichiometric coefficient	μ_2	1.0
Solid heat capacity	$C_{p,s}$	700 J/kg K
Pure fuel heat capacity	$C_{p,f}$	700 J/kg K
Gas heat capacity	$C_{pg,k}$	1000 J/kg K
Heat conductivity between pore sites	λ_{gs}	0.04 w/m K
Heat conductivity between solid sites	λ_s	0.04 w/m K
Pore/surrounding heat transfer coefficient	$h_{L,p}$	4 w/m^2 K
Pore/solid heat transfer coefficient	h_s	80 w/m^2 K
Solid/sourrounding heat transfer coefficient	$h_{L,s}$	4 w/m^2 K
Gas phase velocity	U	0.005 m/s
Diffusion coefficient	D_e	5×10^{-5} m^2/s
Gas viscosity	κ	17.3×10^{-3} cP
Lewis number	Le	1.36×10^{-3}

pressure-drop relationship, in both discrete and continua, the pore-network model can also be viewed, subject to appropriate modifications, as a finite difference version of the continuum model.

(iv) Radiation was neglected. For simplicity, gas-phase and solid-phase thermal conductivities were also taken the same. Accounting for radiation will certainly make the process more realistic, however, at the expense of additional computational cost.

(v) The conductance of a pore was assumed unaffected by the extent of the reaction. Hence, viscous fingering phenomena of the type considered in Ref. [15] were not included.

(vi) While the true kinetics of FC are quite complicated, the simple one-step kinetics used are commonly assumed in the combustion of solid fuels (e.g., see Ref. [26]). Using a more elaborate reaction kinetics model is not necessary for the interpretation of the basic pattern formation.

(vii) Among the many variables that can be spatially distributed, we focused here on the pore-throat size and the amount of fuel. In addition to a random distribution, the first variable was also distributed based on fractional Brownian motion (fBm) statistics, which contain long-range correlations [27].

(viii) In the simulations shown below, the lattice size was typically taken equal to 128×128. This size was small enough for computational expediency but large enough to minimize end effects.

Table I, reprinted for convenience from Ref. [5], contains the nomenclature and typical values associated with the above description. The equations were made dimensionless using the characteristic quantities listed in Table I, resulting in a number of dimensionless groups, including pore-scale Peclet and Nusselt numbers. The latter express heat losses to the surroundings.

The governing equations along with the appropriate boundary conditions were expressed in dimensionless form and solved numerically using a number of linear solvers, including a traditional Successive Over Relaxation (SOR) method, a preconditioned conjugated gradient (PCCG)

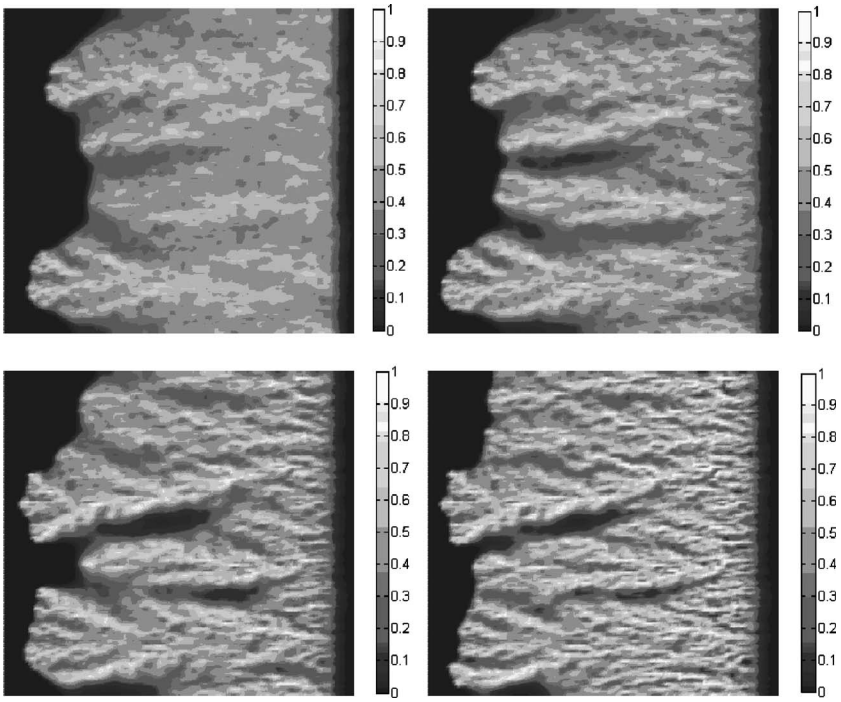

FIG. 2. Snapshots of the spatial profiles of the conversion depth in adiabatic reverse FC (ignition at right, gas injection at left) for randomly distributed throat radii in the interval [0.2, 1.8] for values of the mass Peclet number equal to 0.01, 0.025, 0.05, 0.1 in the four panels, respectively (left-to-right, top-to-bottom). Lighter shades indicate higher conversion depth. Fingering patterns in the sense of regions separating fully burned and unburned fuel did not develop (or developed in a few regions) for this set of parameters. The process is incomplete and the conversion efficiency heterogeneous, with the contrast in the conversion efficiency increasing with the Peclet number. The base parameters of Table I were used with the Lewis number equal to 1.36×10^{-3}.

method and Line Successive Over Relaxation (LSOR) methods. These were used as appropriate. Additional details can be found in Refs. [5,28]. To investigate the possible approach of the system to traveling-wave solutions, the moving coordinate method developed in Ref. [5] was also considered. That technique can address problems for systems whose parameters, such as the pore size, are random functions of space. For example, in a coordinate system moving at velocity v, parameters associated with the pore network become generally random variables in space, and with respect to the moving coordinate ξ they become random variables of time, for example,

$$k(x,y) = k\left(\xi + \int_0^t y(t)dt, y\right). \tag{13}$$

If the relevant parameters depend on all space coordinates, a true traveling steady state does not develop, since in the traveling frame of reference the system receives a fluctuating input, e.g., in the form of the fluctuating pore size. In the asymptotic limit, variables, such as concentration, etc., also become fluctuating functions of time. The technique works well in the more stable case, but it is difficult to apply when the reacting fronts do not span the entire width of the simulation domain. In the moving coordinate method, the velocity is determined by specifying that the transverse average, e.g., of the conversion efficiency, takes a specific value at a fixed axial location.

III. NUMERICAL RESULTS

A. The adiabatic case

Figure 2 shows typical results from numerical simulations of reverse FC, under adiabatic conditions and for four different values of the pore scale Peclet number. The parameter values from Table I were used, with the dimensionless pore throat size randomly distributed using a uniform distribution in the interval [0.2, 1.8]. Because of the fourth-power dependence of the pore flow conductance on the pore radius, the distribution of flow conductances is quite large, hence the disorder is significant, despite the narrow range of pore sizes considered. In the typical application, the Lewis number, defined as $\mathrm{Le}=\alpha_s/D$, and expressing the ratio of the solid thermal diffusively to the gas mass diffusivity, was equal to 1.36×10^{-3} (note the difference with the definition used in Refs. [15,26]). The figure shows four snapshots of the spatial profiles of the conversion depth for values of the mass Peclet number equal to 0.01, 0.025, 0.05, and 0.1, respectively. Lighter shades indicate higher conversion depths. Clearly, the smoldering is incomplete and the conversion efficiency spatially heterogeneous, with the contrast in the conversion efficiency increasing with the Peclet number. However, fingering patterns in the sense of regions separating fully burned from fully unburned fuel did not develop in this adiabatic case (except in some isolated spots). The roughness of the front appears to slightly decrease with an increase in the Peclet number. Smoldering is more or less uniform across the front, although it is intensified at the tips, as shown in the profiles of Fig. 3. This finding is consistent with the stability analysis of Ref. [15], wherein the absence of flow permeability (conductance) enlargement following combustion, the fronts are predicted to be stable, under the assumption of infinitely large Lewis numbers. The tip temperatures in the four panels of Fig. 2 were equal to the following fractions, 0.1770, 0.2085, 0.2052, and 0.2122, respectively, of the fuel adiabatic temperature $T^*=\Delta_r H/C_{pf}$ (which is a property of the pure fuel, and different from the commonly known adiabatic temperature, see also below).

Characteristic temperature and mole fraction patterns (corresponding to the first panel of Fig. 2) are shown in Fig. 3. Reaction is confined near the front, where the oxidant is

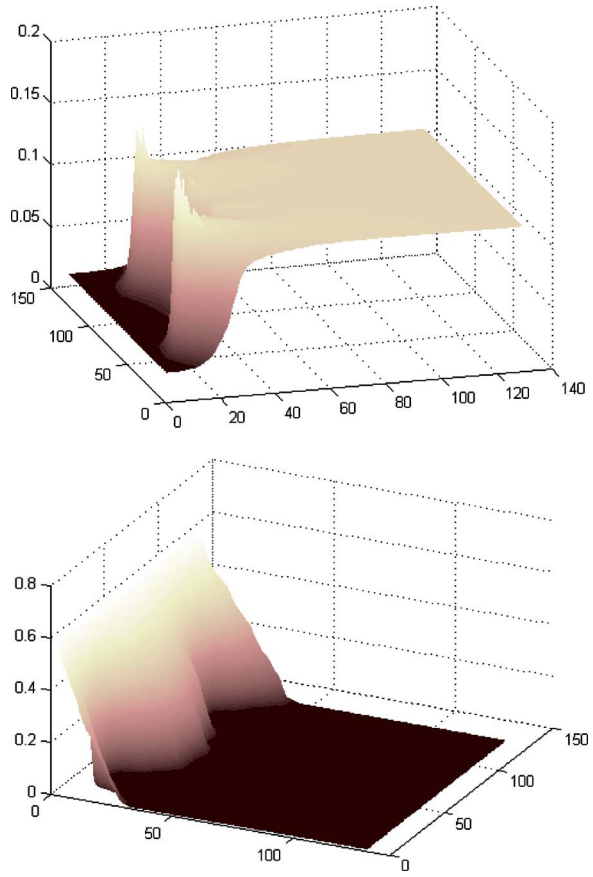

FIG. 3. (Color online) Spatial profiles of temperature (normalized with the fuel adiabatic temperature) (top) and oxidant mole fraction (bottom) in adiabatic reverse FC corresponding to the first panel of Fig. 2 (Pe=0.01, Le=1.36×10^{-3}). The reaction is concentrated at the front and intensified at the tips. Complete oxidant (but not fuel) consumption occurs.

fully consumed. This is typical of all other Peclet number conditions as well. Figure 4 shows transversely averaged profiles of fuel consumption (normalized with respect to full consumption), mole fraction and temperature (normalized with the adiabatic fuel temperature T^*) for the four different panels of Fig. 2. The distance is in terms of lattice spacing units. In general, the higher the Peclet number, the higher the temperature and the larger the mole fraction gradient. Relatively uniform profiles develop behind the front and the process is quasi-one-dimensional. The results on temperature are consistent with the 1D analysis of Lozinski and Buckmaster [26], which predict an increase in the front temperature as the injection rate increases (see also below). The effect of the Peclet number on the conversion efficiency is nonmonotonic, first decreasing and subsequently increasing, as the injection rate increases. This effect is also consistent with the analysis in Ref. [26], which predicts a nonmonotonic dependence of the front velocity on the injection rate. In all simulations, the fuel conversion was incomplete. A full analytical discussion will be given in a subsequent section.

The results in Figs. 2–4 indicate substantial conversion heterogeneity, but not significant fingering. Yet, unstable patterns can emerge if the thermal conductivity is lowered to sufficiently low values. Figure 5 shows results for simulations in which the thermal conductivity was lowered to one-quarter its typical value. In contrast to the higher conductivity case, substantial fingering patterns with a complex morphology emerged. The patterns have the characteristic features of tip splitting, branching, and shielding, associated with viscous fingering in other contexts [13,14]. The lower thermal conductivity leads to much sharper temperature gradients near the tip, as compared to the higher conductivity (e.g., see Fig. 2), hence to the creation of a smaller number of propagating hot spots. The result is reduced ability for ignition and the development of unstable patterns. The low thermal conductivity leads to substantially higher temperatures in the reacting regions, resulting into high fuel conversion inside the fingers. The emergence of unstable patterns at low thermal conductivity is not inconsistent with the analysis of Ref. [15], which predicts stable patterns, but at infinitely large values of the Lewis number.

B. The nonadiabatic case

Patterns corresponding to nonadiabatic reverse FC are shown in Fig. 6 for Pe=0.05 and Nu=0.05. As before, the parameter values from Table I were used, with the dimensionless pore throat size randomly distributed here using a uniform distribution in the interval [0.2, 1.8]. The patterns on conversion depth show very distinct features of a fingering instability. The fingers undergo branching, shielding and tip-splitting, and bypass, leaving unreacted, a significant fraction of the fuel in place. These features are quite similar to patterns of viscous fingering in porous media or a Hele-Shaw cell (e.g., see Refs. [13,14]). The instability appears to be almost the same with the experimentally reported on paper smoldering in a Hele-Shaw cell by Zik *et al.* [10] and Zik and Moses [11], even though the two processes are not identical. All reaction activity is concentrated near the tip of the fingers, where the temperature is high and the oxidant is available, the rest of the medium participating very little in the reaction process. Substantial variation of the temperature occurs at the front, with hot spots at the active finger tips. The temperature decays away from the tip toward the ambient, reflecting heat losses to the environment. For the conditions of Fig. 6, the temperature at the tip was about 0.1873 of the fuel adiabatic temperature. While smaller than in the corresponding case of Fig. 5, the conversion efficiency in each finger was significant. The oxidant is fully consumed near the tip of the finger. Properties at the fingers, such as the conversion depth and the tip temperature, fluctuate slightly around a steady-state value. Contrary to forward FC [28], the fuel is not fully consumed even in places where the supply of oxidant is not limited.

The emergence of a well-defined fingering pattern suggests that mechanisms similar to those in Zik and Moses [11] are in effect. To probe these mechanisms, we used the model to study the sensitivity of the process to a number of variables, specifically, the effect of the injection velocity (Peclet number), and of the heat losses. In many ways, we tried to mimic the experiments by Zik *et al.* [10] and Zik and Moses [11], even though the analogy between experiments and simulations is not exact (in the experiments fluid flow oc-

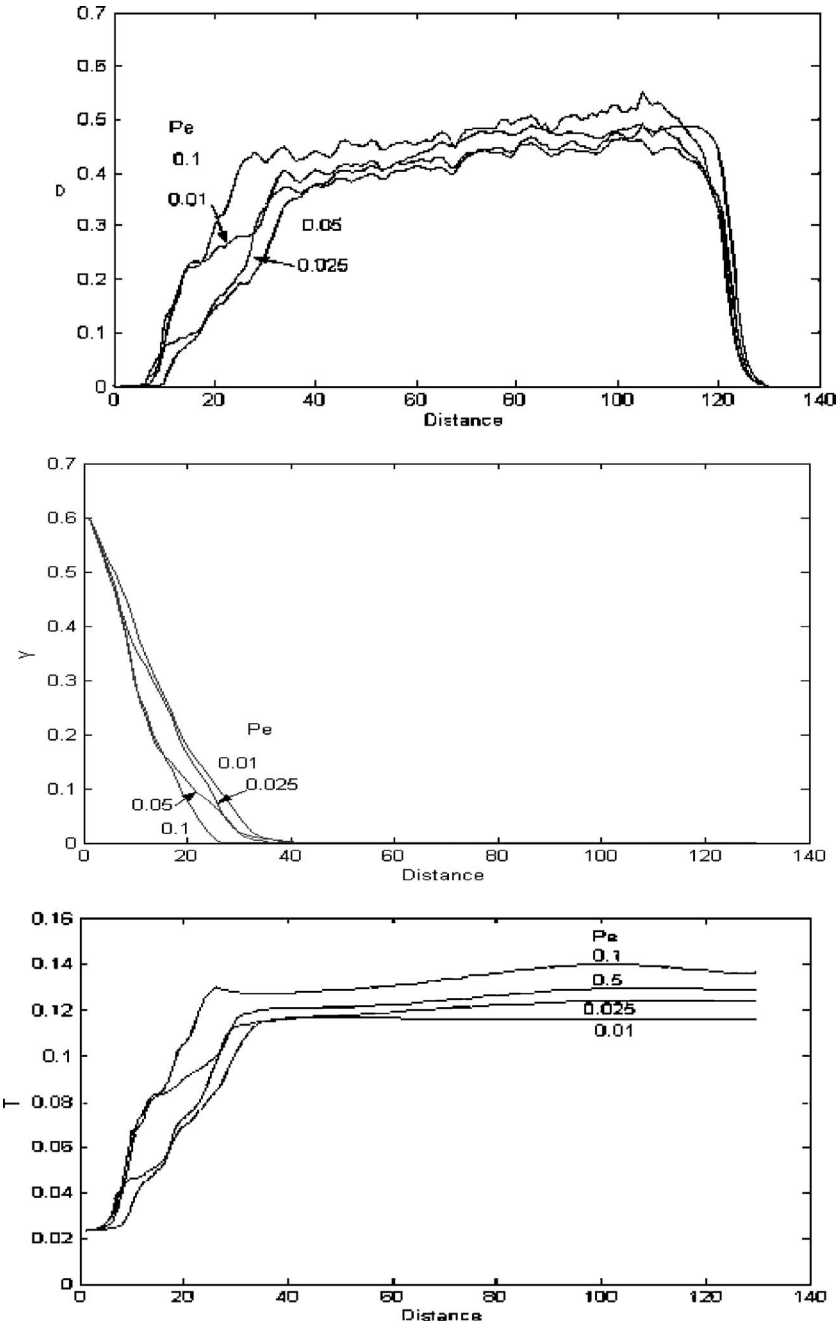

FIG. 4. Transversely averaged profiles of fuel consumption (normalized with full consumption), mole fraction and temperature (normalized with the fuel adiabatic temperature) for the four different panels of Fig. 2. The distance is in terms of lattice spacing units. In general, the higher the Peclet number, the higher the conversion efficiency and the temperature. Relatively uniform profiles develop behind the front.

curred mainly in the space left between the smoldering paper and the Hele-Shaw cell, while in the simulations flow occurred within the pores of the porous medium).

1. Effect of injection velocity

The injection velocity affects pattern formation, as it changes the relative lengths of mass and thermal fields. In addition, high values of the velocity can induce extinction [29]. In this section we report on simulations conducted at different values of the injection rate. The corresponding mass Peclet numbers varied in the range 0.01 to 0.1, implying diffusion-control regime at the pore-network scale. Two cases were considered, one in which the dimensionless bond radius was distributed as white noise in the interval [0.2, 1.8] and another in which it was held constant to 1.0. All other properties were held constant. Fingering in the constant radius case was initiated by a small fluctuation of the ignition temperature.

Patterns for the two cases are shown in Figs. 7 and 8. Common to the figures are intense fingering patterns and the dependence of the pattern on the injection velocity (expressed in the figures through the mass Peclet number). The finger spacing appears to decrease with the Peclet number, with the variation well captured in a narrow range of the Peclet number (between 0.01 and 0.1). The finger width is less sensitive to the velocity. Pronounced tip splitting occurs at higher values of the Peclet number in the case of distributed pore radius (Fig. 7). Even though the morphology is very dense in the higher Pe limit, considerable amount of

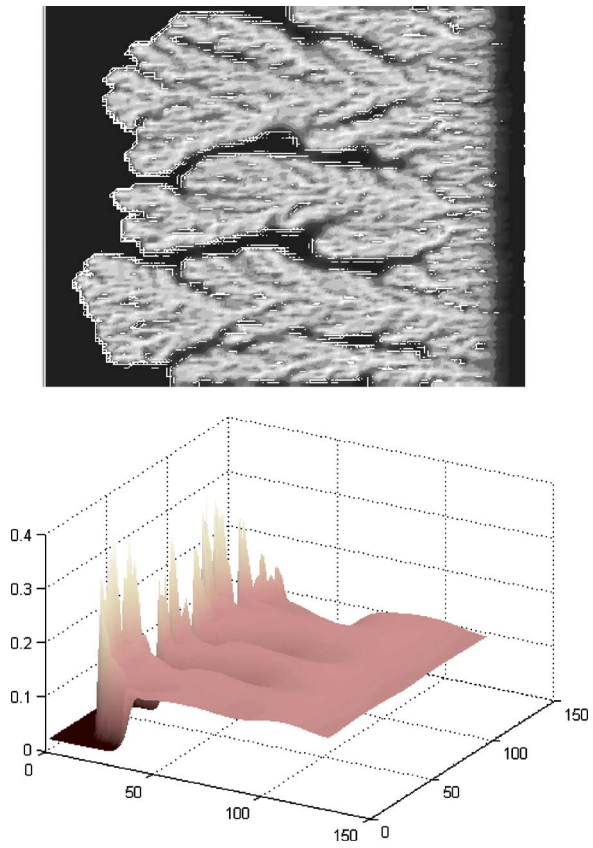

FIG. 5. (Color online) A snapshot of the spatial profile of the conversion depth in adiabatic reverse FC for randomly distributed throat radii in the interval [0.2, 1.8] (top panel) and the corresponding temperature, expressed as a fraction of the fuel adiabatic temperature (bottom panel) for mass Peclet number equal to 0.05 and a Lewis number equal to 3.4×10^{-4} (one-quarter the value in Fig. 2). Lighter shades in the fingers indicate higher conversion depth. Contrasted to Fig. 2, substantial fingering patterns develop. The base parameters of Table I were used. Note the substantially high temperature at the propagating tips, which sustain the growth of the fingers and leads to a locally high conversion efficiency.

bypassing occurs and a fraction of the fuel remains unburned (Fig. 7). Conversely, very limited tip splitting is observed in the homogeneous case, where the fingers appear to grow almost parallel to one another (Fig. 8). The tip splitting observed as the fingers approach the injection end is likely an end effect. In the simulations in the heterogeneous case (Fig. 7), the tip temperature fluctuates around a steady value which reached about 0.25 of the fuel adiabatic value, for all Peclet numbers except the first. The trend (increase of the temperature with the Peclet number) is somewhat similar to the adiabatic case, although the tip temperatures are indeed higher in the presence of heat losses. The fuel conversion inside each finger was complete, expect in the limit of high injection rates, where conversion within a finger is incomplete. Similar results were observed for the homogeneous case, the overall conversion efficiency in the homogeneous case being slightly higher than in the heterogeneous case (0.5958 vs 0.5354). The tip temperature appears to increase with the Peclet number, except in the high-Peclet number for the homogeneous case, where it decreases, reflecting the almost uniform front. The fingering behavior, particularly for the heterogeneous case, is similar to that in the experiments of Refs. [10,11], even though our model did not simulate exactly that configuration. One important difference with the results in Refs. [10,11] is the upper value of the Peclet number, where the simulations show compact behavior, and which is about two orders of magnitude lower (however, this may well reflect the different length scales used in the definition in the two different works, and which were approximately two orders of magnitude different). With the present set of parameters, the transition between an isolated finger and the compact case occurred in a relatively small window spanning only one order of magnitude (between 0.01 and 0.1) in the Peclet number.

2. Effect of heat losses

In their experiments, Zik and Moses [10] studied thermal effects on the width of isolated fingers in two different ways: (1) by varying the distance between the two plates, and (2) by varying the thickness and material of the supporting plate onto which the paper (to be smoldered) was pasted. In our simulations, we mimicked these configurations by varying two parameters: (1) the strength of the heat losses to the surroundings, through variations in the Nusselt number; (2) the volumetric fraction of the fuel (which essentially expresses the rate of heat release, for it determines the adiabatic temperature). In this section we examine the sensitivity to the first. As was noted, heat losses are of the volumetric type, as the lattice is two dimensional.

Figure 9 shows fuel conversion patterns for different values of the heat loss Nusselt number. As the heat loss rate intensifies, the fingers become distinct. It appears that there exists a common backbone in all patterns (here noticed as long as $\mathrm{Nu}<0.04$), with the contrast in conversion around the backbone increasing with the increase in the Nusselt number. Heat losses make the interface between consumed and unreacted regions much sharper. At the same time, they act to eliminate weak hot spots, and thus reduce the number of fingers. In such cases, the distance of fingers may no longer be controlled by the diffusion of oxygen. The tip temperature was generally found to increase with the rate of heat losses (equal to 0.1635, 0.1968, 0.1873, 0.2162 of the fuel adiabatic temperature in the four panels of Fig. 9). This rather unexpected result reflects a combination of facts, as increased rate of heat losses leads to a smaller number of hot spots, with concentrated activity and hence a higher rate of heat generation. As the number of hot spots decreases, the concentration gradients toward them increase, thus making for a robust reverse combustion process at these places, despite the increased rate of heat losses. Figure 10 shows results corresponding to relatively strong heat losses ($\mathrm{Nu}=0.08$). In the case of weak heat losses (Fig. 6) the oxidant is fully consumed at the fingers, and significant tip-splitting occurs, forming many local hot spots. With strong heat losses (Fig. 10), on the other hand, the oxidant is not totally consumed and there is a continuous oxidant leakage through the fingered region. This leakage increases with the strength of the heat losses. Temperature profiles are very sharp, and the reaction activity is limited to very small regions near the

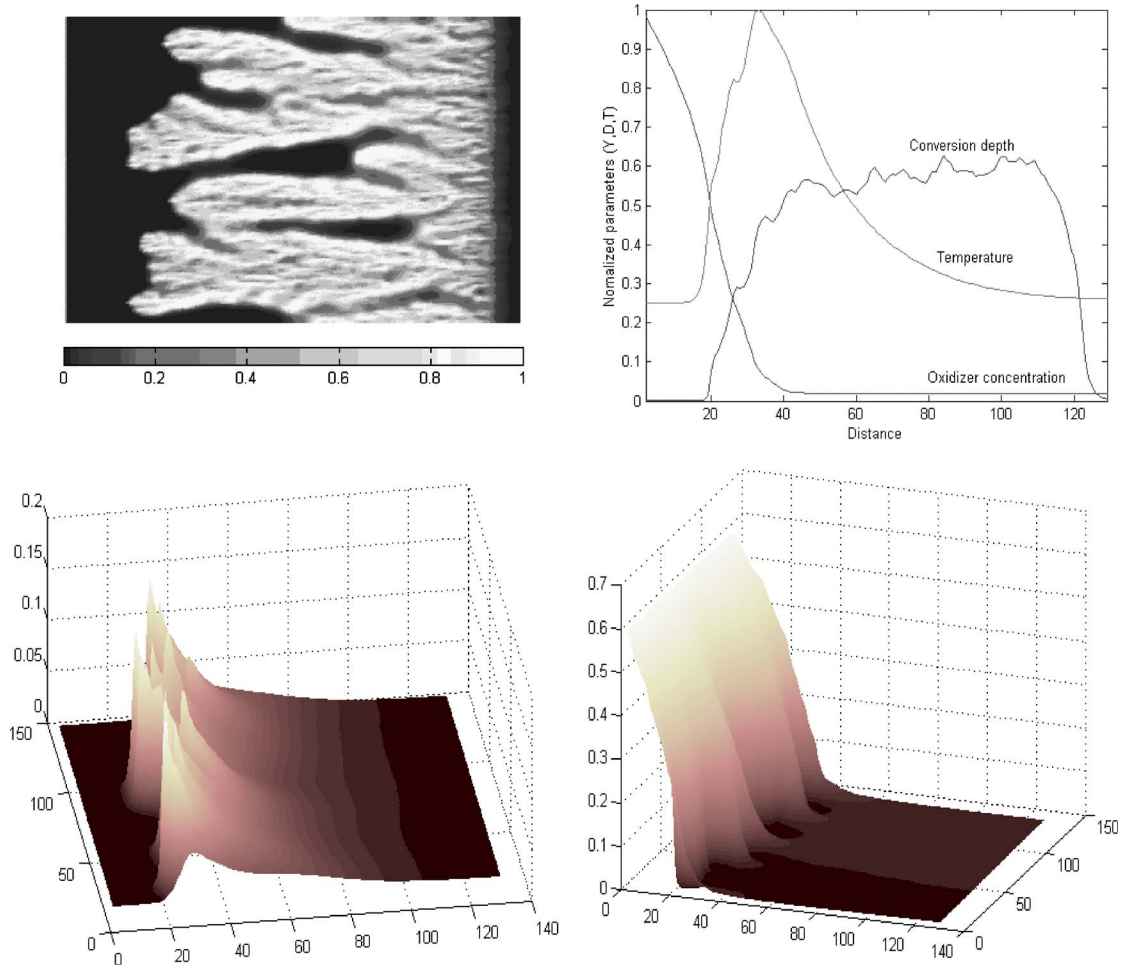

FIG. 6. (Color online) Snapshots of the spatial profiles of the conversion depth, temperature and oxidant mole fraction, and of the transversely averaged variables, in a typical nonadiabatic reverse FC (ignition at right, injection at left) for randomly distributed throat radii in the interval [0.2, 1.8]. The base parameters of Table I were used with Pe=0.05 and Nu=0.05. Lighter shades in the fingers indicate higher conversion extent. Note the emergence of a well-defined fingering pattern. In this simulation, all the oxidant was fully consumed at the back of the fingers with resulting high conversion efficiency inside the fingers. The temperature in the third panel is expressed as a fraction of the fuel adiabatic temperature (see text). The tip temperature reached 0.1873 of the fuel adiabatic temperature. The oxidant concentration in the fourth panel is expressed in terms of its mole fraction in the gas phase. In the second panel, all variables were normalized with the largest value. With the exception of the temperature profile, the transversely averaged features are similar to the adiabatic case.

finger tips, where concentration gradients are strong. As a result, the oxidant is consumed at the reacting tips, and overall it leaks through the front largely unreacted. This causes a decrease in the average conversion efficiency. The patterns change from tip splitting to more like isolated fingers, as the heat loss intensity increases.

3. Spatially correlated (fBM) conductances

For completeness, we also show a numerical simulation, where the pore-size distribution is correlated in space. As is the case in other aspects of unstable growth, spatial correlations can produce drastically different patterns. The effect is illustrated in simulations with an fBm distribution (Fig. 11). The conversion patterns are dramatically different from those for the uncorrelated, randomly distributed radius. The extensive fingering by tip splitting shown in the previous patterns is substantially reduced, the process evolving now in terms of a few connected fingers. Finger propagation occurs preferentially in the spatially connected high flow conductance regions, leaving unreacted substantial regions, through which the gas phase oxidizer leaks unreacted. The effect of the Hurst exponent is not very significant and consists of simply sharpening the contrast between reacted and unreacted regions. The problem can be roughly approximated as reverse FC in a layered medium with a high permeability channel. Due to the higher oxidant supply in that region, the reaction front propagates preferentially along this fracture. As with other unstable growth processes in disordered media, flow heterogeneities have a dramatic influence on patterns, as long as mass transfer is the limiting factor.

IV. DISCUSSION

In this section we will next discuss the results obtained above in the context of the available theories for reverse FC and unstable pattern formation. We will interpret the quasi-

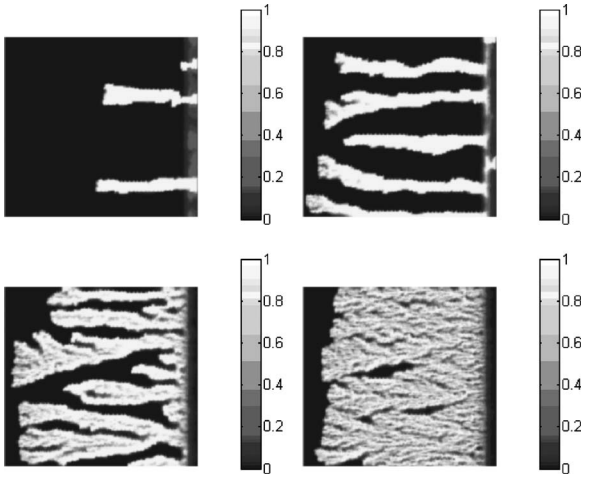

FIG. 7. Snapshots of the spatial profiles of the conversion depth in nonadiabatic reverse FC (ignition at right, injection at left) for randomly distributed throat radii in the interval [0.2, 1.8] for different values of the mass Peclet number equal to 0.01, 0.025, 0.05, 0.1 in the four panels, respectively (left-to-right, top-to-bottom). Lighter shades in the fingers indicate higher conversion depth. The finger spacing decreases as the injection velocity increases. Isolated fingers propagate at low Peclet numbers. Tip splitting is observed at higher values of the velocity (third and fourth panels). (The tip splitting observed as the fingers approach the injection end is likely an end effect.) An almost compact front develops at the highest Peclet number of 0.1 (fourth panel). The tip temperatures in the four panels were equal to the following fraction of the fuel adiabatic temperature, 0.1848, 0.2535, 0.2457, and 0.2548, respectively. The base parameters of Table I were used with Nu=0.05.

one-dimensional results of the adiabatic case at high thermal conductivities (Figs. 2–4) using a one-dimensional (1D) solution along the lines of Lozinski and Buckmaster [26]. For the fingering patterns, we will test the scaling relations (3) and (4) of Zik and co-workers [10,11], but we will also attempt a different interpretation based on the solvability conditions for Laplacian growth.

A. 1D solution for reverse FC

Consider first 1D reverse FC. We will analyze this process because it allows us to obtain analytical insights into the overall problem. Lozinski and Buckmaster [26] provided an asymptotic methodology, based on an expansion in terms of the Zeldovich number. This approach is common to problems of FC (e.g., see application by our group in forward FC, Akkutlu and Yortsos [29]). Using the notation of the latter, accounting for a temperature effect in the pre-exponential factor of the reaction rate (which was neglected in Ref. [26] but kept here), and assuming a continuum formalism, 1D reverse FC is modeled as follows [see schematic of Fig. 12]. Outside the reaction zone, temperature and mole fraction profiles have the exponential behavior

$$\theta = 1 + (\theta_f - 1)\exp(A\xi) \quad \text{for } \xi < 0 \text{ and } \theta = \theta_f \text{ for } \xi > 0, \tag{14}$$

$$Y = Y_i[1 - \exp(\mathrm{Le}\, B\xi)] \quad \text{for } \xi < 0 \text{ and } Y = 0 \text{ for } \xi > 0. \tag{15}$$

Here, θ is the rescaled temperature (dimensionless with the ambient) and θ_f is the front temperature, a parameter that

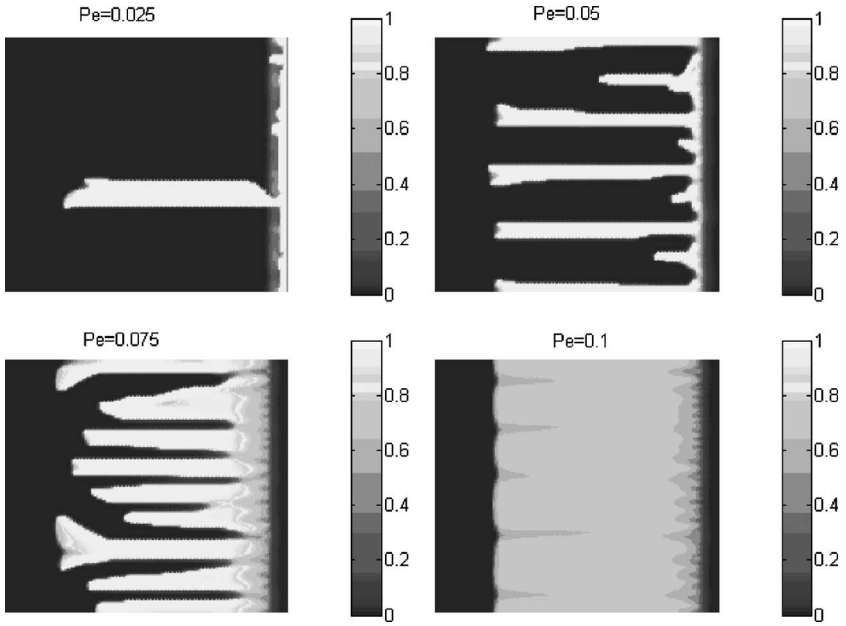

FIG. 8. Snapshots of the spatial profiles of the conversion depth in nonadiabatic reverse FC (ignition at right, injection at left) for a unimodal distribution of the dimensionless throat radii and for different values of the mass Peclet number equal to 0.025, 0.05, 0.075, and 0.1 in the four panels, respectively (left-to-right, top-to-bottom). Lighter shades in the fingers indicate higher conversion depth. The finger spacing decreases, while the finger width is less sensitive, as the injection velocity increases. Significant less tip splitting is observed compared to the disordered case of Fig. 6. (The tip splitting observed as the fingers approach the injection end is likely an end effect.) An almost compact front develops at a Peclet value of 0.1. The tip temperatures in the four panels were equal to the following fraction of the fuel adiabatic temperature, 0.1851, 0.2029, 0.2009, and 0.1634, respectively. The base parameters of Table I were used with Nu=0.05.

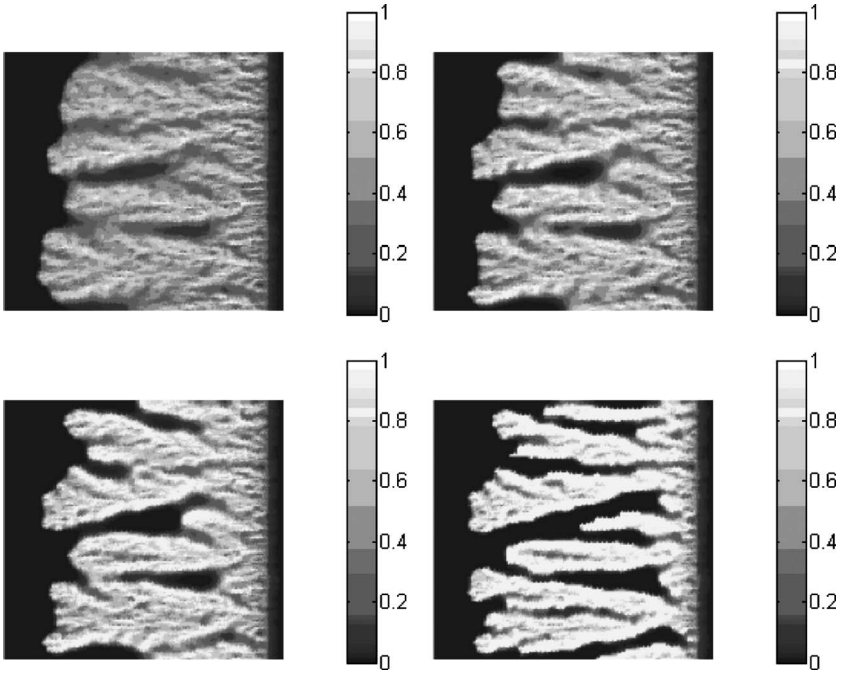

FIG. 9. Snapshots of the spatial profiles of the conversion depth for different values of the heat losses (Nu=0.00, 0.001, 0.02, 0.04, from left-to-right, top-to-bottom) in nonadiabatic reverse FC for randomly distributed throat radii in the interval [0.2, 1.8]. Lighter shades in the fingers indicate higher conversion depth. As the heat loss rates increase, the fingering pattern becomes sharper. The tip temperatures in the four panels were equal to the following fraction of the fuel adiabatic temperature, 0.1635, 0.1968, 0.1873, 0.2162, respectively. The base parameters of Table I were used with Pe=0.05.

must be determined. Parameter $A=a\rho u-v>0$ is approximately equal to the negative of the dimensionless (and negative) front velocity, v, except where the latter is small. Here, u is the dimensionless flow velocity (equal to 1, in the absence of compressibility effects). We also defined a rescaled gas density ρ (normalized with its value at the inlet) and denoted by $a \ll 1$ the ratio of gas to solid volumetric heat capacities. Likewise, $B=u-\phi v>0$, where ϕ is porosity. In the above, the front velocity [also denoted as $\tilde{u}$ in Eq. (4)] was made dimensionless with the injection velocity V. The above representation assumes full consumption of the oxidant at the front. We note that the exponential dependence of the profiles shown in (14) and (15) is consistent with the transversely averaged profiles of Fig. 4.

Inside the reaction zone, the mole fraction approaches zero, the space coordinate must be stretched ($\xi=\varepsilon X$) and temperature and mole fraction variables must be perturbed around the front temperature and the zero value of the mole fraction at the front, respectively (see Refs. [26,29]). We take $\theta=\theta^0+\varepsilon\theta^1+\ldots$, $Y=\varepsilon Y^1+\ldots$, where superscripts 0 and 1 denote leading-order and perturbation, and the small parameter was defined as $\varepsilon=RT_f^2/ET_0$. The perturbations in the temperature and the mole fraction satisfy the equations

$$\frac{\partial^2\theta^1}{\partial X^2}+\varepsilon q\Phi=0, \tag{16a}$$

$$\frac{\partial^2 Y^1}{\partial X^2}-\varepsilon\,\mathrm{Le}\,\sigma\Phi=0 \tag{16b}$$

while the mass balance for the fuel reads

$$-v\frac{\partial\eta^0}{\partial X}=\varepsilon\Phi. \tag{16c}$$

The reaction rate is $\Phi=(a_sY^1/\theta_f)\exp\theta^1$, where we also introduced the notation $\theta_f=\theta^0$. Parameter a_s contains information on the kinetic constants [29]. In addition, we defined the rescaled stoichiometric coefficient $\sigma=\mu\rho_f/\rho_g$ and the dimensionless heat release rate $q=\Delta_rH\rho_f/(1-\varphi)\rho_sC_{ps}T_0$. In forward FC, the dimensionless adiabatic temperature is equal to $1+q$. Here, the fuel adiabatic temperature referred to in the preceding section is approximately equal to $T^*/T_0=[(1-\varphi)\rho_s/\rho_f]q$. The above equations are to be integrated subject to the boundary conditions

$$\eta^0\to 0,\theta^1\to-\infty,Y^1\to-\infty \quad \text{as } X\to-\infty, \tag{17a}$$

$$\eta^0\to\eta_\infty,\theta^1\to 0,Y^1\to 0 \quad \text{as } X\to 0. \tag{17b}$$

Inner and outer regions are coupled with the jump conditions,

$$\left.\frac{\partial\theta^1}{\partial X}\right|=\left.\frac{\partial\theta}{\theta\xi}\right|=qv\eta_\infty=-\frac{q}{\sigma\,\mathrm{Le}}\frac{\partial Y^1}{\partial X}=-\frac{q}{\sigma\,\mathrm{Le}}\frac{\partial Y}{\partial\xi}. \tag{18}$$

Using the second and last of the above, and the profiles from (14) and (15) we find

$$\theta_f=1+\frac{q}{\sigma}\frac{BY_i}{A} \tag{19}$$

which shows that the front temperature depends on injection and front velocities through the two parameters A and B. The third and last of (18) gives an expression for the fuel conversion behind the front

$$\eta_\infty=-\frac{1}{\sigma}\frac{BY_i}{v}, \tag{20}$$

which also shows a dependence on injection and front velocities. Using Eq. (16) we can integrate the profiles within the reaction zone to obtain an additional equation that relates the front velocity to the front temperature. In the notation of Ref. [29] this reads as follows:

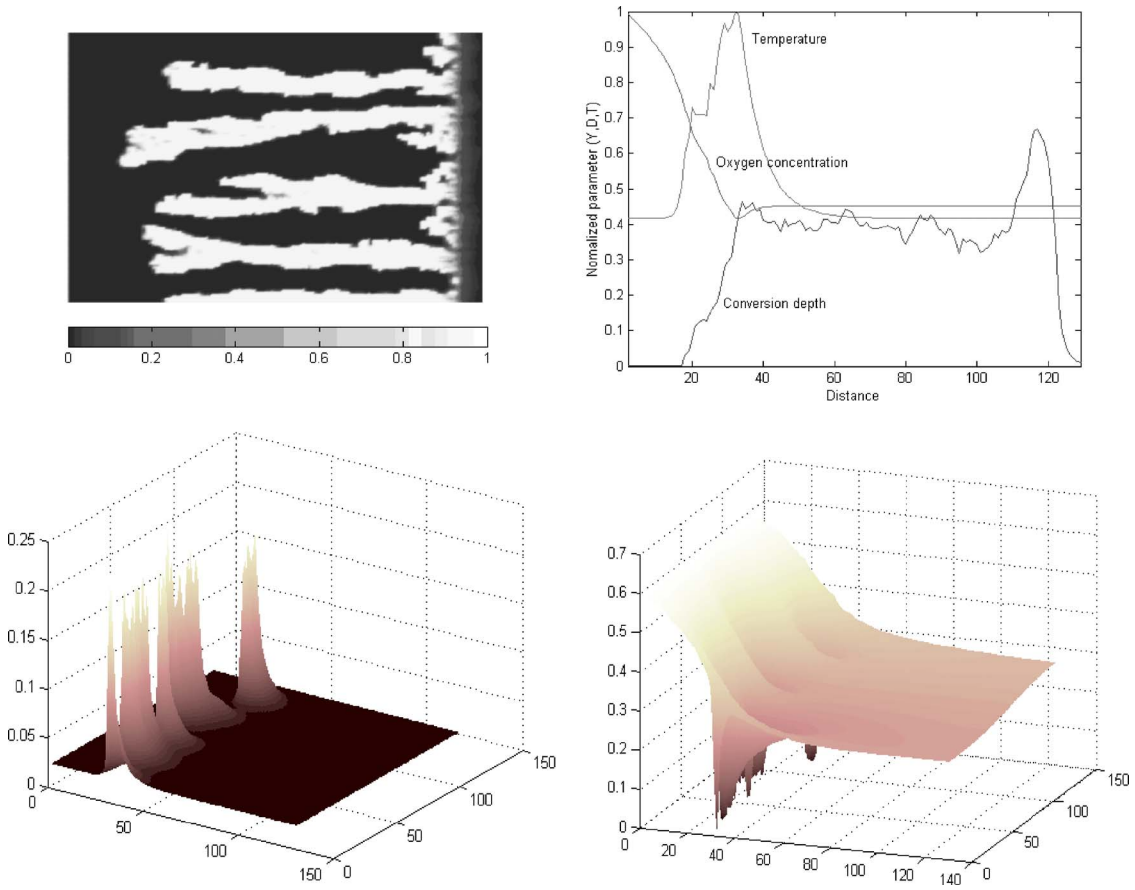

FIG. 10. (Color online) Snapshots of the spatial profiles of the conversion depth, temperature, and oxidant mole fraction, and of the transversely averaged variables, in a typical nonadiabatic reverse FC for randomly distributed throat radii in the interval [0.2, 1.8]. The base parameters of Table I were used with Pe=0.05 and Nu=0.08, corresponding to strong heat losses. Lighter shades in the fingers indicate higher conversion depth. The temperature in the third panel is expressed as a fraction of the fuel adiabatic temperature. The tip temperature reached 0.2292 of the fuel adiabatic temperature. The oxidant concentration in the fourth panel is expressed in terms of its mole fraction in the gas phase. In the second panel, all variables were normalized with the largest value. Note the significant leakage of the oxidant through the regions between the fingers. The low temperature environment away from the tips concentrates all reaction activity near the finger tips, where the concentration gradients of the oxidant are large.

$$\frac{A^2}{2}(\theta_f - 1)^2 = \frac{q}{\gamma}\sigma \,\mathrm{Le}\,\mathrm{Re}\,\theta_f^3 \exp\left(-\frac{\gamma}{\theta_f}\right), \tag{21}$$

where we defined the dimensionless parameter $\mathrm{Re} = \tilde{a}_s \alpha_s k_0 Y_i P / qEV^2$. The simultaneous solution of Eqs. (21) and (19) leads to the front velocity and the front temperature. As Lozinski and Buckmaster [26] showed, in this solution, the front temperature increases monotonically with the injection velocity, while the front velocity has a nonmonotonic dependence, first increasing and subsequently decreasing with the injection velocity. The predictions of a monotonic increase of the front temperature with injection rate are consistent with the profiles of Fig. 4. Of course, a direct numerical comparison is not warranted, as the process in Fig. 4 is 2D, while the assumption made here is that of a 1D geometry. The dependence of the fuel consumption efficiency according to Eq. (20) predicts first a decrease, and then a subsequent increase, with the injection rate. This is also qualitatively evidenced in Fig. 4. We note that in the presence of heat losses, the 1D solution remains valid, except that parameter A in Eqs. (14), (19), and (21) must be replaced with $A' \equiv \frac{1}{2}(A + \sqrt{A^2 + 4h}) > 0$, where we introduced the dimensionless heat transfer coefficient $h \equiv \mathrm{Nu}(\mathrm{Le}/\mathrm{Pe})^2$.

B. Analysis of pattern formation in 2D reverse FC

Subsequently, a quantitative analysis of the patterns (finger spacing and finger width) was attempted using the approach of Zik and Moses [11]. In our analysis, the width of a finger was measured in terms of the number of pore lengths along a fixed value of the transverse coordinate, within which the fuel conversion depth is higher than a prescribed cutoff, arbitrarily taken as 0.05. The complement was defined as the finger spacing. The ensemble mean of the so-obtained values over the region swept by the reaction front (with regions close to the boundaries omitted) was then computed and used to denote the average finger spacing (or width). The average values from the simulation results for various cases are plotted in Fig. 13 as a function of $\mathrm{Pe}^{-1/2}$ [as suggested by Eqs. (3) and (4)]. At first glance, the predictions from the equations are satisfied well, at least in a qualitative sense. In

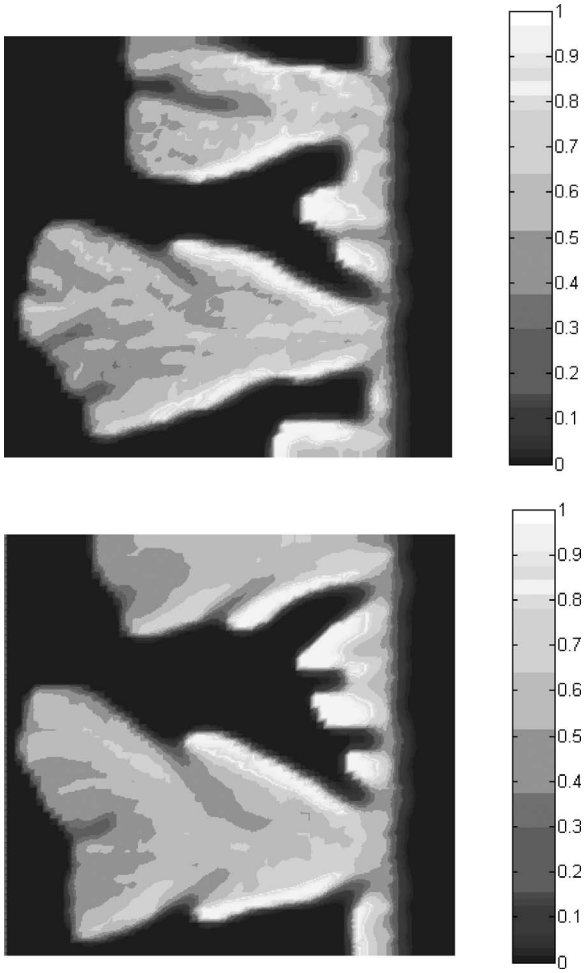

FIG. 11. Snapshots of the spatial profiles of the conversion depth for spatially correlated throat-radius size distributions using fractional Brownian motion statistics and corresponding to two different values of the Hurst exponent ($H=0.1$ and $H=0.7$ in the top and bottom panels, respectively). Nonadiabatic reverse FC for radii in the interval [0.2, 1.8], with Nu=0.05, Pe=0.01 and the parameters of Table I. Lighter shades in the fingers indicate higher conversion depth.

particular, the width of the fingers does not appear to be sensitive to the Peclet number, while a linear regression of the data shows that the spacing can be approximated as a linear function of $\mathrm{Pe}^{-1/2}$. However, the quantitative agreement with the theory is rather poor. The theory predicts a negative intercept equal to the finger width, which is not the case in the figure. The theoretical slope, according to Eq. (3), must be equal to $\sqrt{\tilde{w}/A}$, which if used in Fig. 13 gives $A \approx 0.25$. However, for the pore-network model, the stoichiometric parameter A is approximately equal to $A=0.0046$, in rather poor agreement. It is apparent that a different approach may be necessary.

An alternative to interpreting the pore-networks results is by following the finger selection theory based on solvability conditions for Laplacian growth [13]. Consider the growth of a finger in a continuum and in the symmetric geometry shown in the schematic of Fig. 12. No-flux conditions are assumed at the sides. Assuming a steady state, traveling with

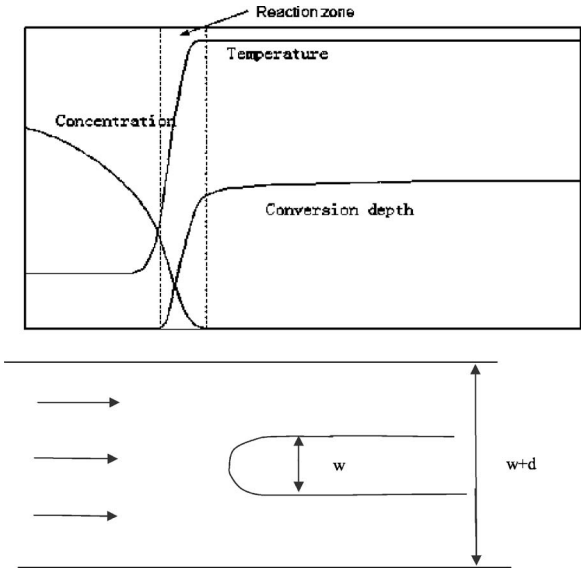

FIG. 12. Schematics for the analysis of the 1D (top panel) and 2D (bottom panel) reverse combustion configurations. Ignition at right, injection at left. In the bottom panel a single finger is shown with no-flux conditions applied at the lateral boundaries. This geometry is assumed to represent a unit cell, for example, of the bottom-right panel in Fig. 9. The width and the spacing of the finger is denoted in dimensionless notation.

velocity $-v$, and transforming to coordinates traveling with the finger ($\xi=x+vt$) the mass balance of the oxidant in dimensionless notation is

$$\rho B \frac{\partial Y}{\partial \xi} = \frac{1}{\mathrm{Le}} \nabla \cdot (\rho \nabla Y) - \sigma \Phi(Y, \theta), \tag{22}$$

where the notation of the 1D formulation was used. In the above, we neglected transverse flow associated with tem-

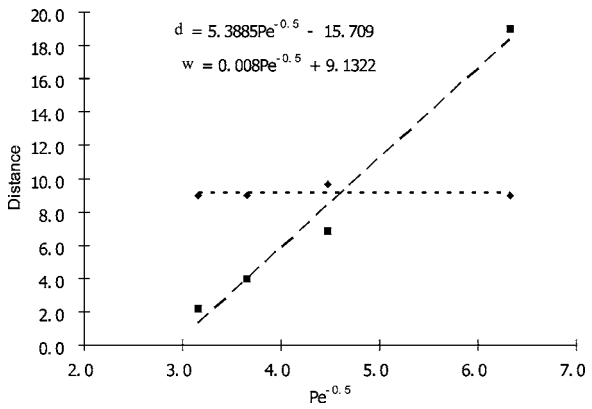

FIG. 13. The dependence of the average spacing between the fingers d and the finger width w (in units of pore lengths) as a function of the inverse square root of the Peclet number from the pore-network simulations. Shown also are the equations from linear regression. The distance between fingers can be approximated as a linear function of $\mathrm{Pe}^{-1/2}$, while the width of the fingers is not strongly affected and stays close to about nine pore lengths. However, the slope of the curve is not consistent with the theory.

perature gradients. The mass balance on the fuel reads

$$-v\frac{\partial \eta}{\partial \xi}=\Phi(Y,\theta) \tag{23}$$

while the overall gas mass balance reads $\rho B=$const. We proceed next, by neglecting variations in density in the diffusion term in Eq. (22). Then, taking the volume integral of the above two equations over the entire domain gives, assuming no-flow conditions at the lateral boundaries gives,

$$(w+d)\rho B(Y_\infty - Y_i) = -\sigma \int \Phi dV, \tag{24}$$

$$-v\,\eta_\infty w = \int \Phi dV. \tag{25}$$

Eliminating the reaction term and denoting the stoichiometric coefficient as $a^*=\sigma\eta_\infty/(Y_i-Y_\infty)$, it is not difficult to show the following relation:

$$-v=\frac{1}{\left(a^*\frac{w}{d+w}-\varphi\right)}=\frac{1}{(a^*\lambda-\varphi)}, \tag{26}$$

where the ratio $\lambda=w/(d+w)$ is the relative thickness of the finger. Equation (26) is the analog of the mass balance (1). The difference is that in Eq. (1), the product ρB was approximated as $\rho B\approx 1$, under the acceptable assumption that the front velocity is considerably smaller in magnitude than the injection velocity (see also Ref. [26]). Under this condition, Eq. (26) becomes

$$-v\approx\frac{1}{a^*\lambda}. \tag{27}$$

Zik and Moses [11] used Eq. (2), which is qualitatively but not quantitatively exact, and which in the present notation reads

$$-v=\frac{1}{(d+w)\mathrm{Pe}}. \tag{28}$$

Then, assuming constant finger width w, one finds

$$\lambda\approx\sqrt{\frac{w\,\mathrm{Pe}}{a^*}}. \tag{29}$$

Equation (29) suggests an increase of the finger relative thickness with the square root of the Peclet number. Figure 14 shows that, while Eq. (29) fits the Zik and Moses [11] theory reasonably well, it is not as effective in fitting our numerical results (for the admittedly different problem of reverse FC). Specifically, the different degrees of disorder represented in the figure give much different slopes and intercepts for the straight line fit represented in (29), and in fact such lines do not pass from the origin, or they have a much different slope than that required by the theory. Nonetheless, the qualitative trend of an increasing relative width with the square root of the Peclet number is indeed obeyed. However, even if accepted, this relation will ultimately lose validity, as

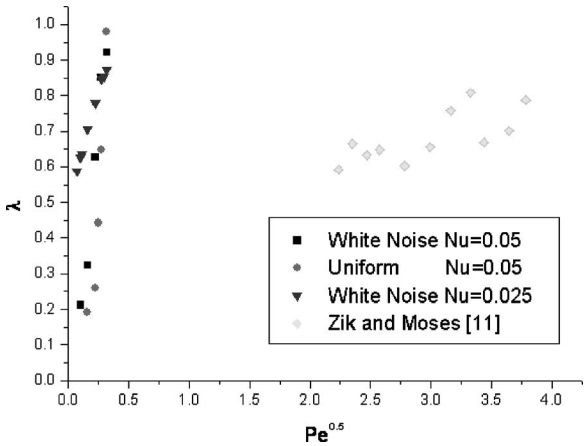

FIG. 14. The dependence of the relative finger width on the square root of the Peclet number from the pore-network simulations and from the data of Zik and Moses [11], based on the theory of the latter. A generally monotonic relation is shown, although it is not evident that our simulation results can be fitted well to the straight line predicted by Eq. (29).

the relative finger width must saturate to a theoretical maximum of one at high Peclet numbers.

To provide an alternative relation, we seek progress using Laplacian growth, which has been extensively discussed in the literature. Here, we will not attempt to derive a solvability condition for the full process. Rather, under conditions of mass transfer control, we will borrow from existing results. The closest example to the present problem of reverse FC is solidification in a confined geometry, such as a capillary [13,14]. At small values of the Peclet number, growth is similar to the Saffman-Taylor finger, the selection of which was thoroughly examined by McLean and Saffman [30] and Vanden-Broeck [31]. Following Pelce [14], a solvability condition is obtained through the following relation:

$$\kappa(\lambda)=\frac{4d_0\pi}{(-v+1)l\,\mathrm{Pe}(d+w)^2(1-\lambda)^2}. \tag{30}$$

In the above, the relation $\kappa(\lambda)$ is a universal solvability curve, obtained independently for Laplacian growth in specific geometries (e.g. Refs. [30,31]), d_0 is a chemical length, playing the role of a capillary coefficient and l is a characteristic length. Use of an equation, such as (30), obviates the need for the uncertain equation (28). We will use (30) for the present problem of reverse FC and under the assumption that the oxidant concentration is fully depleted, in which case the analogy to solidification can hold. Clearly, this pertains only to a restricted region in terms of heat losses or other parameters, as discussed in the results above. In terms of the present variables and geometry, and after suitable rearrangements to reflect a continuum description, Eq. (30) can be rearranged to the following approximate expression:

$$\kappa(\lambda)=\frac{4d_0\pi\lambda(a^*\lambda-\varphi)}{lw^2a^*\,\mathrm{Pe}(1-\lambda)^2}. \tag{31}$$

Figure 15 shows data from the pore-network simulations, plotted in terms of the rescaled parameter, $\kappa'=\kappa l/4d_0\pi$,

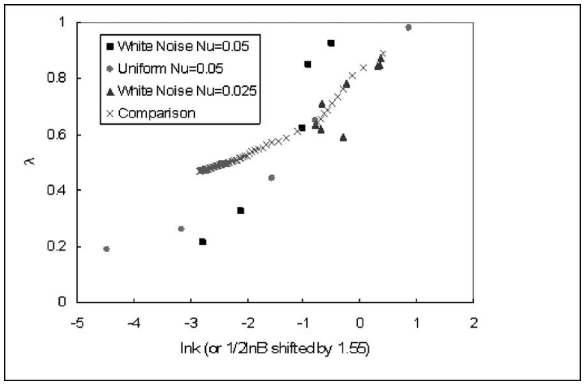

FIG. 15. The dependence of the relative finger width on the modified parameter $\kappa' = \kappa l / 4 d_0 \pi$, denoted in the figure as k, according to the solvability condition expressed in Eq. (31), plotted in semilog coordinates. Results from pore-network simulations of reverse FC under nonadiabatic conditions and for two different pore size distributions (white noise and unimodal) are shown. Plotted also (symbol ×) is the experimental relation of Tabeling *et al.* [32], with the horizontal axis being the parameter $B^{1/2}$ shifted by a constant factor. The two sets are in reasonable agreement at higher values of the relative finger width (higher than about 0.5) and for smaller heat losses.

where we absorbed the various unknown geometric constants. The results have generic features common to those for Laplacian growth. For example, superimposed on the figure is the experimental curve of Tabeling *et al.* [32], reprinted from Pelce [14], which pertains to immiscible viscous fingering in a Hele-Shaw cell. The latter results were plotted in a logarithmic plot vs parameter B of Tabeling *et al.* [32], which is proportional to the inverse of the capillary number of the displacement. There is a certain similarity of the pore-network results for RC in a pore network with the experimental results for viscous fingering in a Hele-Shaw cell, when the relative finger width is above 0.5, and the heat losses are not strong. The trends are consistent with the fact that Peclet number and capillary number often act in the same direction in providing an effective capillarity to interface growth, even though they correspond to different phenomena, see also Pelce [14]. The similarity fails at smaller values of the relative finger width, however, which is understandable, given that under these conditions, the finger distance is large, the oxidant is not fully consumed and the above selection expression fails.

V. CONCLUSIONS

In this paper, reverse FC was investigated with a 2D pore-network model. Included in the model were all relevant mechanisms of fluid flow, mass transfer and reaction kinetics in the pore space and of heat transfer in the pore and the solid space. Heat losses to the ambient were also included. The results showed distinct fingering patterns, expected for reverse FC, and driven primarily by diffusional instability. This is opposite to the problem of forward FC, where diffusion is stabilizing. Thus, at low values of the Peclet number, reverse combustion generates unstable patterns, while the opposite is true for forward combustion. This difference between forward and reverse processes is also common in other applications driven by Laplacian growth [e.g., contrast diffusion-limited-aggregation (DLA) and compact pattern formation, also known as anti-DLA, in viscous fingering, melting and solidification, etc.].

We investigated the effects of various parameters to the patterns obtained, including the Peclet number, the heat loss intensity and the effect of pore size disorder. Our simulations showed that oxidant supply, through the Peclet number, is the most important controlling factor for pattern behavior. The other important factor is the ability of a single hot spot to sustain itself. The latter is affected by the heat release, heat loss rates as well as heat conduction. A better understanding of their interaction needs further work. In the experiments in Ref. [11] it was noted that the thickness of the Hele-Shaw cell has strong influence on the width of fingers, and was explained by a corresponding heat loss effect. Our simulations partly agree with this argument. Heat loss variation within a suitable range will maintain the overall pattern unchanged and only help to demarcate more clearly the interface between burnt and unreacted regions. Sufficiently strong heat losses, on the other hand, can eliminate any weak hot spots and produce much sparser and thicker fingers. This difference may be partly due to the limited size of the computational domain, but the detailed mechanism of heat loss should be inspected more carefully. Conversely, higher heat release rates sustain more and smaller hot spots, thus producing more fingers.

The pattern selection observed was interpreted in two different ways, one based on the arguments of Zik and Moses [11], but for the slightly different problem of slow paper combustion in a Hele-Shaw cell, and another by making an analogy to the solvability problem in Laplacian growth. Qualitatively, the finger spacing was found to increase with $\mathrm{Pe}^{-1/2}$, while the relative finger width was also an increasing function of $\mathrm{Pe}^{1/2}$, consistent with the theory in Ref. [11]. For quantitative results, we applied a version of the solvability problem in Laplacian growth, which was found to be in reasonable agreement when the heat losses are not too strong.

[1] M. Prats, *Thermal Recovery*, SPE Monograph Series, Dallas, TX, Society of Petroleum Engineers (SPE, AIME, 1982).
[2] S. Hwang, A. S. Mukasyan, A. V. Rogachev, and A. Varma, Combust. Sci. Technol. **123**, 165 (1997).
[3] S. Hwang, A. S. Mukasyan, and A. Varma, Combust. Flame **115**, 354 (1998).
[4] T. J. Ohlemiller, Prog. Energy Combust. Sci. **11**, 277 (1985).
[5] C. Lu and Y. C. Yortsos, AIChE J. **51** (4), 1279 (2005).
[6] A. P. Aldushin and B. J. Matkowsky, Combust. Sci. Technol. **133**, 293 (1998).

[7] M. R. Booty and B. J. Matkowsky, Combust. Sci. Technol. **80**, 231 (1991).
[8] D. A. Schult, A. Bayliss, and B. J. Matkowsky, SIAM J. Appl. Math. **58**, 806 (1998).
[9] M. Conti and U. M. B. Marconi, Physica A **312**, 381 (2002).
[10] O. Zik, Z. Olami, and E. Moses, Phys. Rev. Lett. **81**, 3868 (1998).
[11] O. Zik and E. Moses, Phys. Rev. E **60**, 518 (1999).
[12] S. L. Olson, H. R. Baum, and T. Kashiwagi, *Finger-like Smoldering over Thin Celluloid Sheets in Microgravity*, Twenty-Seventh Symposium on Combustion (The Combustion Institute, 1998), p. 2525.
[13] P. Pelce, *Dynamics of Curved Fronts* (Academic, Boston, 1988).
[14] P. Pelce, *Theorie des Formes de Croissance*, Savoirs Actuels (EDP Sciences, 2000).
[15] J. A. Britten and W. B. Krantz, Combust. Flame **60**, 125 (1985).
[16] M. J. Blunt, M. D. Jackson, M. Piri, and P. H. Valvatne, Adv. Water Resour. **25**, 1069 (2002).
[17] M. L. Hoefner and H. S. Fogler, SPE paper 13564 (1985).
[18] M. Sahimi and T. T. Tsotsis, J. Catal. **96**, 552 (1985).
[19] Y. C. Yortsos and M. M. Sharma, AIChE J. **32**, 46 (1986).
[20] R. Mann, Catal. Today **37**, 331 (1997).
[21] U. A. El-Nafaty and R. Mann, Chem. Eng. Sci. **54**, 3475 (1999).
[22] C. Satik and Y. C. Yortsos, J. Heat Transfer **118**, 455 (1996).
[23] M. Prat, Chem. Eng. J. **86**, 153 (2002).
[24] A. Yiotis, A. G. Boudouvis, A. K. Stubos, I. N. Tsimpanogiannis, and Y. C. Yortsos, AIChE J. **50**, 2721 (2004).
[25] C. Lu and Y. C. Yortsos, Ind. Eng. Chem. Res. **43**, 3008 (2004).
[26] D. Lozinski and J. Buckmaster, Combust. Flame **102**, 87 (1995).
[27] J. Feder, *Fractals* (Plenum, New York, 1988).
[28] C. Lu, Ph.D. dissertation, University of Southern California, 2002.
[29] I. Y. Akkutlu and Y. C. Yortsos, Combust. Flame **134**, 229 (2003).
[30] J. W. McLean and P. G. Saffman, J. Fluid Mech. **102**, 455 (1981).
[31] J. M. Vanden-Broeck, Phys. Fluids **26**, 2033 (1983).
[32] P. Tabeling, G. Zocchi, and A. Libchaber, J. Fluid Mech. **177**, 67 (1987).